Charge-induced pattern displacement in E-beam lithography

Arat, Kerim T.; Klimpel, Thomas; Zonnevylle, Aernout C.; Ketelaars, Wilhelmus S.M.M.; Heerkens, Carel Th H.; Hagen, Cornelis W.

DOI
10.1116/1.5120631

Publication date
2019

Document Version
Final published version

Published in
Journal of Vacuum Science and Technology B: Nanotechnology and Microelectronics

JVST B
Journal of Vacuum Science & Technology B

Charge-induced pattern displacement in E-beam lithography

Cite as: J. Vac. Sci. Technol. B **37**, 051603 (2019); https://doi.org/10.1116/1.5120631
Submitted: 19 July 2019 . Accepted: 13 August 2019 . Published Online: 16 September 2019

Kerim T. Arat, Thomas Klimpel, Aernout C. Zonnevylle, Wilhelmus S. M. M. Ketelaars, Carel Th. H. Heerkens,, and Cornelis W. Hagen

Charge-induced pattern displacement in E-beam lithography

Kerim T. Arat,[1,a)] Thomas Klimpel,[2] Aernout C. Zonnevylle,[3]
Wilhelmus S. M. M. Ketelaars,[3] Carel Th. H. Heerkens,,[1] and Cornelis W. Hagen[1]
[1]*Faculty of Applied Sciences, Delft University of Technology, Lorentzweg 1, 2628CJ Delft, The Netherlands*
[2]*GenISys GmbH, Eschenstrasse 66, 82024 Taufkirchen, Germany*
[3]*Raith B.V., De Dintel 27a, 5684PS Best, The Netherlands*

(Received 19 July 2019; accepted 13 August 2019; published 16 September 2019)

Electron beam lithography (EBL) requires conducting substrates to ensure pattern fidelity. However, there is an increasing interest in performing EBL on less well-conducting surfaces or even insulators, usually resulting in seriously distorted pattern formation. To understand the underlying charging phenomena, the authors use Monte Carlo simulations that include models for substrate charging, electron beam-induced current, and electric breakdown. Simulations of electron beam exposure of glass wafers are presented, exposing regular patterns which become distorted due to charge-induced beam deflection. The resulting displacements within the patterns are mapped and compared to experimental displacement maps obtained from patterns in PMMA resist on glass substrates. Displacements up to several hundreds of nanometers were observed at a primary beam energy of 50 keV. Also, various scan strategies were used to write the patterns, in the simulations as well as the experiments, revealing their strong effect on pattern distortion, in shape and in magnitude. A qualitative, in some cases even quantitative, good agreement was found between the simulations and the experiments, providing enough confidence in Monte Carlo simulations to predict charge-induced pattern displacement and shape distortion and to find smart scan strategies to minimize the effects of charging. *Published by the AVS.*
https://doi.org/10.1116/1.5120631

I. INTRODUCTION

Electron beam lithography (EBL) is used for the production of a wide range of applications such as the production of superconducting nanowires[1] and quantum dots[2] because it combines very high resolution and flexible patterning capabilities.[3–5] However, when the sample is not sufficiently conducting, charging-related differences occur on the designed pattern.[6] One of these differences is due to the unintended deflection of the primary beam, which causes pattern distortion.[7] The literature discusses a few techniques to solve this problem: adding a charge dissipation layer,[8,9] using a conductive polymer,[10,11] using variable pressure conditions,[12] or utilizing the critical energy.[13] So far, these techniques were not well adopted by the semiconductor industry, except the first one because of its practicality and low cost. However, using a coating layer introduces extra process complexity,[14] a loss of resolution due to the increased electron scattering volume, and it does not solve the issue entirely, especially for thick resists.[15]

In addition to the methods mentioned above, some authors investigated the effect of the scan (writing) strategy[16] on the charging effect. However, this is quite a demanding experimental work because finding the right strategy is based on a trial and error method and restricted to the specific application. In the literature, modeling studies using Monte Carlo simulations are reported, which are aimed at providing a general solution for a given layout prior to the experimental fabrication.[17–20] However, these studies are either based on empirical electron-matter scattering models or do not take charge redistribution into account.

The goal of this work is to use a Monte Carlo simulator that simulates charging by including first principle scattering models, electric fields, and charge redistribution models.[21] Specific test patterns were defined in PMMA resist on glass wafers. The same patterns were also obtained simulating electron beam exposure of a glass wafer and then compared to the experimentally obtained patterns. Furthermore, the influence of different writing strategies on the patterns was investigated.

II. MODELING

A. Monte Carlo simulator

In this study, we have used a Monte Carlo simulator, *virtualSEM*, to simulate the charge-induced effects on the primary electron beam. The first version of the simulator[22] included semiempirical scattering models and electric fields. Later, first principle scattering models and charge redistribution models were included in the simulator.[21]

For modeling of the inelastic scattering, there are two choices in the simulation: (i) the dielectric function theory (DFT) which is a first principle model[23,24] and (ii) the continuous slowing down approximation (CSDA) which is a semiempirical model.[22,25] Although the first principle modeling is a rigorous approach, it comes at a price when considering the simulation speed. In this work, initially, we used the DFT model for some of the simulated patterns

Note: This paper is part of the Conference Collection: The 63rd International Conference on Electron, Ion, and Photon Beam Technology and Nanofabrication (EIPBN 2019).
[a)]Electronic mail: k.t.arat@tudelft.nl

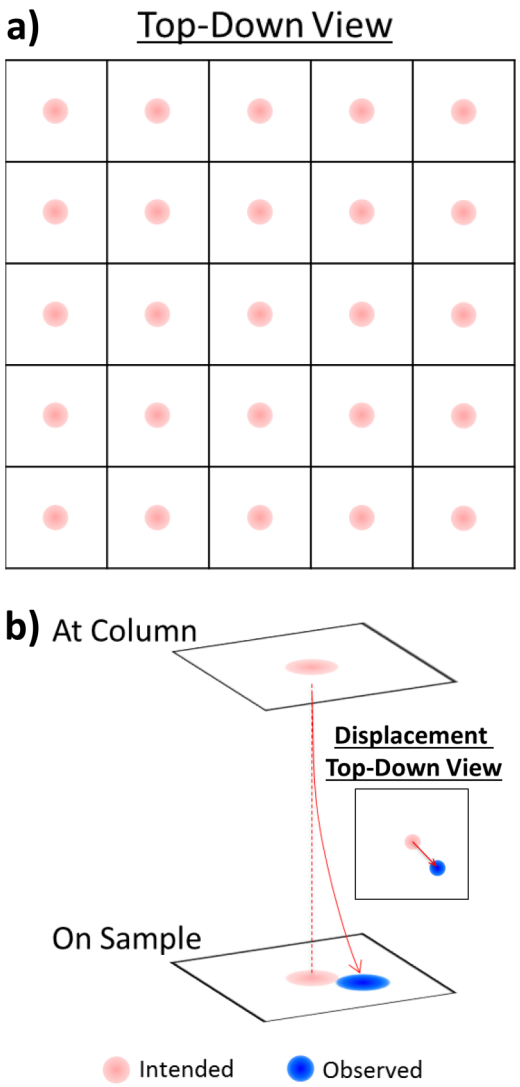

FIG. 1. Test pattern. (a) A schematic drawing of the exposed dot array (5 × 5) is shown in a top-down view. The light gray dots (red dots in the color online version) are the intended points of exposure. (b) The intended and deflected trajectory of the primary electron beam is presented. On the right-hand side, a top-down view of the dot displacement is shown.

studied to understand the effects of the charging. Later, we preferred to use the CSDA model for all simulations to reduce the simulation time. We will address the validity of this approach in Sec. II C.

B. Test pattern: Dot matrix

Here, we focus on the deflection of the primary electrons in vacuum due to substrate charging[7,26] in high energy EBL. The test pattern we chose consists of a square array of dots such that the effect of the deflection can be easily determined by measuring the displacement of the dots with respect to their position in the design (see Fig. 1). Here, each dot represents the result of a single point exposure of the glass wafer by a high energy electron beam.

The array of dots can be written using various writing orders. To investigate the effect of scan strategy on the charge patterns, we have applied four different strategies, as shown in Fig. 2.

The pattern dimensions are $4.5 \times 4.5\,\mu m^2$ (in x and y directions), which corresponds to the subfield size of the e-beam tool used in the experiments. Furthermore, all patterns were written for two different pitches, or dot spacings: 500 nm (9 × 9 dots) and 250 nm (17 × 17 dots).

C. Simulations

To obtain experimentally measurable displacements, we have used a 50 keV electron beam instead of 100 keV, as the 50 keV beam is more sensitive to electrostatic fields (E-fields). A range of exposure doses was simulated up to $250\,\mu C/cm^2$. To exaggerate the effect of the charging, we used exposure doses higher than usual.[16]

As a sample for the simulations, we chose to use glass, i.e., SiO_2, without a resist layer. At 50 keV, the penetration depth of the beam electrons is in the order of micrometers,[27] which means that most of them end up in the substrate. Therefore, we assumed that most of the displacement is due to the substrate charging,[7,28] neglecting charging of a resist layer.

In Fig. 3, the displacement map is shown for the *Meander* mode, at $128\,\mu C/cm^2$ and at 250 nm pitch (17 × 17 dots). The design layout of exposure points is shown as regular grid of circles (the blue circles in the color online version) and the actual landing positions as a nonregular grid of circles (the red circles in the color online version). The arrows indicate the displacement direction, and their size and color correspond to the magnitude of the displacement. The background color has a similar function for better visualization. The writing starts from the bottom left in the *Meander* mode

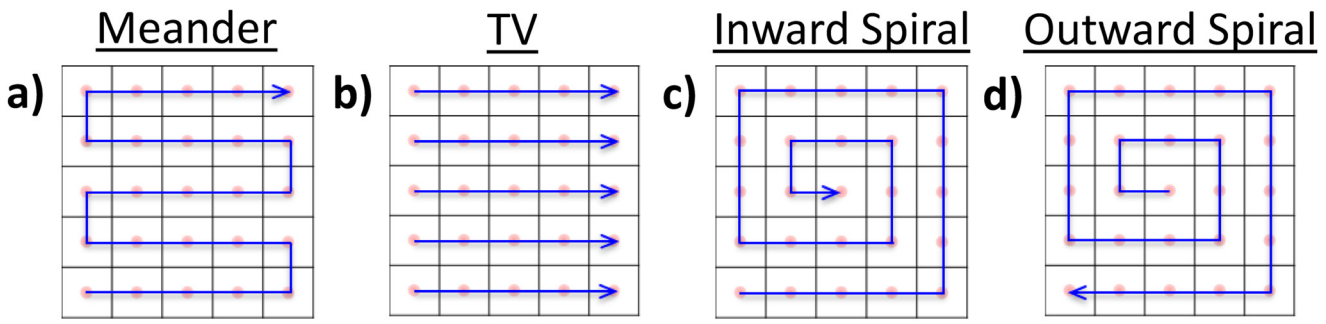

FIG. 2. Four scan strategies (a) *Meander*, (b) *TV* (Raster), (c) *Inward Spiral*, and (d) *Outward Spiral* are shown from left to right. The dots are exposed in the order indicated by the blue arrows starting from the bottom left and ending top right except for the *Outward Spiral* mode, which starts in the middle and ends at the bottom left.

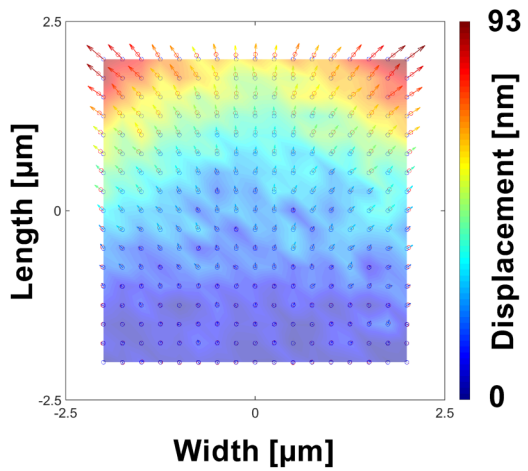

FIG. 3. Displacement map of the *Meander* mode. The maximum displacement is 93 nm at 128 μC/cm^2 and at a pitch of 250 nm (17 × 17 dots).

(see Fig. 2). The displacement is very low in the beginning since the number of trapped charges is still low enough to not influence the beam trajectory. The size of the displacement increases as the beam continues to charge the sample toward the top of the array. The displacement is maximum at the top corners because the amount of deposited charge on the outside of the corners is much smaller than on the inside of the corners, creating stronger E-fields in the diagonal directions.

The displacement maps of all four scanning modes are compared in Fig. 4. The maximum displacement is 93 nm for *Meander*, 93 nm for *TV*, 105 nm for *Outward Spiral*, and 40 nm for *Inward Spiral*. In Fig. 4, below the maps, cartoons are drawn indicating the deformation of the square arrays due to charging. Depending on the application, it can be crucial where the main displacements occur within the pattern. For instance, if a square structure is desired, then the *Inward Spiral* mode provides the best match because all displacements occur inside the pattern as depicted by Fig. 4, leaving the edges of the pattern unaltered.

Figure 4 shows that the scan mode has a significant impact on the landing positions. In the *Meander* and *TV* modes, the bottom of the pattern was exposed first, and the trapped charges repel the beam, away from the exposed area, such that the displacement vectors point in the direction away from the center of the already written area. In *Outward Spiral* mode, the charges are trapped mostly in the center of the pattern from the beginning of the exposure. This repels the beam away from the center in all directions, depending on the location of the point of exposure.

In *Inward Spiral* mode, the beam exposes the borders first starting at the bottom left corner. During this first pass, the amount of trapped charge is not enough to significantly deflect the beam. The amount of trapped charge increases when the beam exposes a new spot, but it exposes another point soon after that, on the opposite side of the pattern, minimizing the lateral component of the electrostatic field. For example, there are undisplaced exposures in the middle of the pattern since the electrostatic fields around these points cancel each other in the x and y directions.

As the charge accumulates, the resulting field will not only deflect the electron beam in x and y directions but also influence the electrons in the z direction, in other words, affect the landing energy of the beam. In Fig. 5, the simulated surface potential at the end of the array exposure is shown. The potential takes values as high as −16 kV, and the surface potential acts as a deceleration field. That means the landing energy of the 50 keV beam drops to 34 keV toward the end of the array exposure, thereby enlarging the deflection of the beam in the x and y directions, as slower electrons are deflected more.

This decrease in landing energy has another important effect on the exposure. At lower energy, the primary beam shows

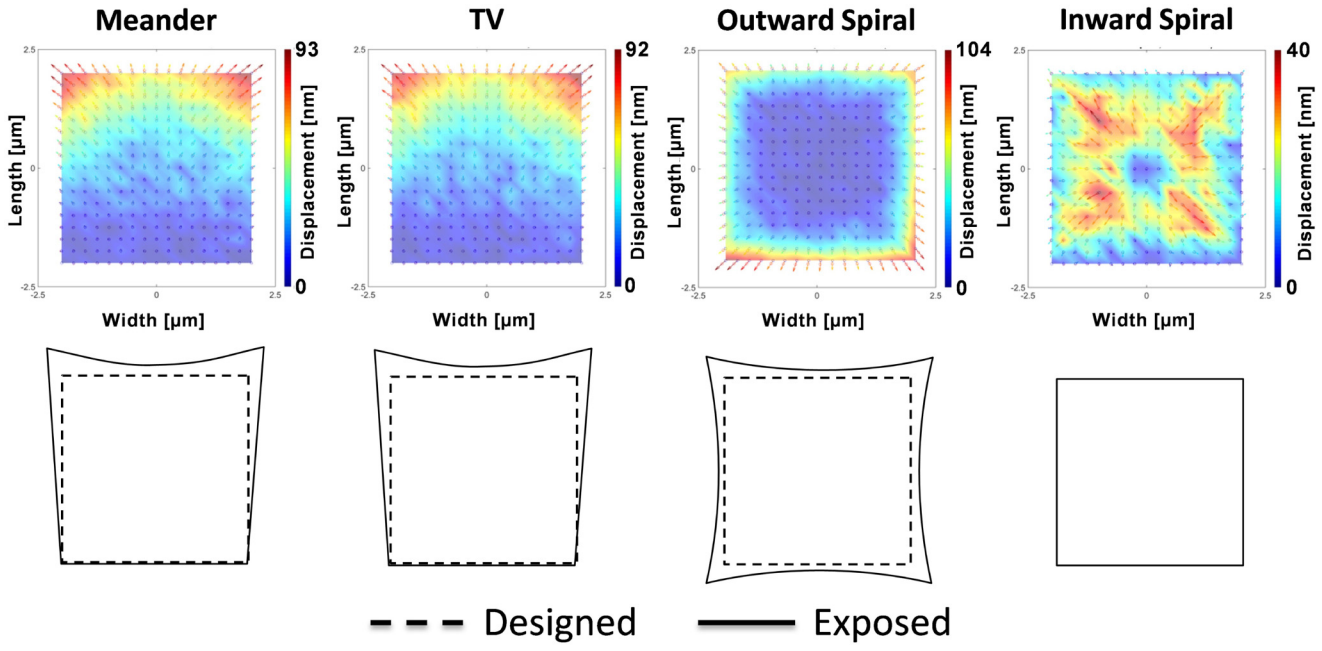

FIG. 4. Displacement effect on the borders of the patterns.

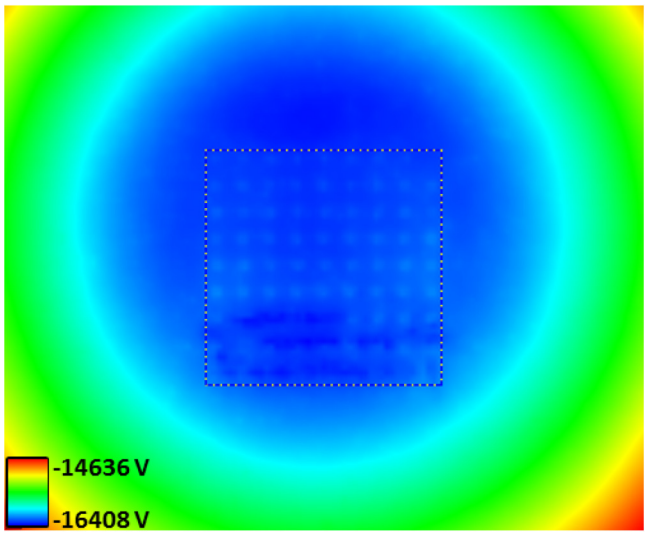

FIG. 5. Surface potential at the end of the array exposure, in Meander scan for 128 μC/cm^2 and a pitch of 500 nm (9 × 9 dots). The color bar shows the maximum (−146 36 V) and minimum (−164 08 V) values of the potential at the surface. The field of view is 10 × 10 μm^2, and the dashed square (4.5 × 4.5 μm^2) indicates the exposure area.

more beam broadening.[29,30] Furthermore, the electrons penetrate less, so their scattering volume is closer to the surface, resulting in a larger intersection of the scattering volume and the substrate surface. As a result of this, we see that the center of the negative potential area in Fig. 5 is located above the center of the exposure area. Also, it is expected that the dots in the upper rows of the array have a larger size than those in the lower rows. We will verify this experimentally.

As promised above, we now address how the simulation results shown are influenced by the particular choice of an inelastic model used in the simulator: model (1) the CSDA and model (2) the DFT.

The two different models resulted in qualitatively very similar displacement maps independent of dose, except for the magnitude of the displacement, which does depend on the dose (see Fig. 6). The effect of statistical (shot) noise was also observed in Fig. 6(b), which leads a slightly different symmetry between Figs. 6(a) and 6(b). Figure 7 shows that the CSDA model results in a displacement twice as big as that of the DFT model for *Meander* mode.

It is worth noting that the displacement map is independent of the dose in the simulations unless dielectric breakdown occurs. The exposure dose changes the magnitude only.

III. EXPERIMENT

To experimentally verify the simulation results, glass wafers were (i) coated with resist, (ii) exposed, (iii) developed, and (iv) inspected.

A. Fabrication of the patterns

A 200 μm (±20 μm) thick insulating SiO_2 wafer (2 × 2 cm^2) was spin-coated with 950k-PMMA resist. The expected resist thickness is 200 nm. After spin-coating, the sample was baked at 175 °C for 30 min. Also, a conducting reference

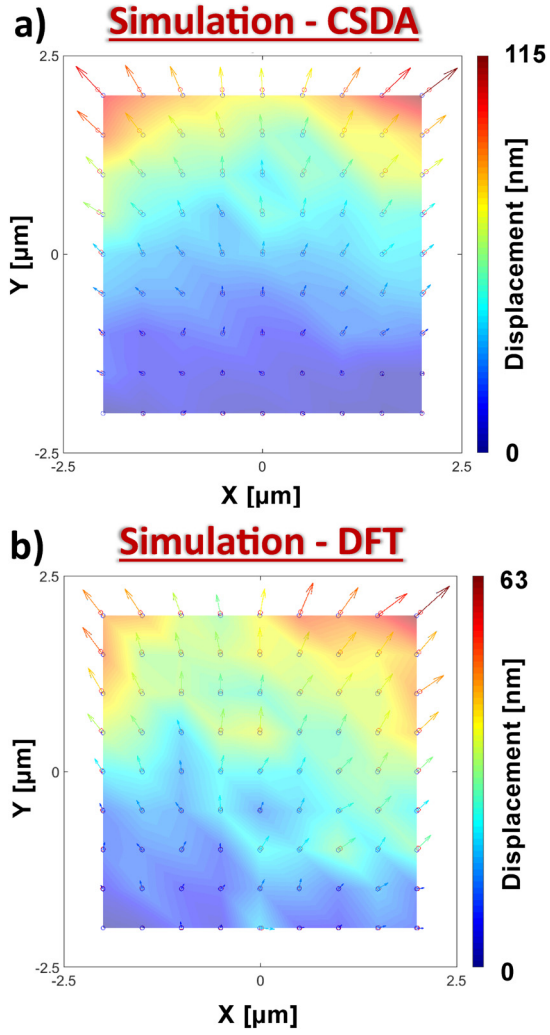

FIG. 6. Sensitivity of the displacement maps to the choice of inelastic scattering model at 128 μC/cm^2 for the *Meander* mode: (a) CSDA vs (b) DFT.

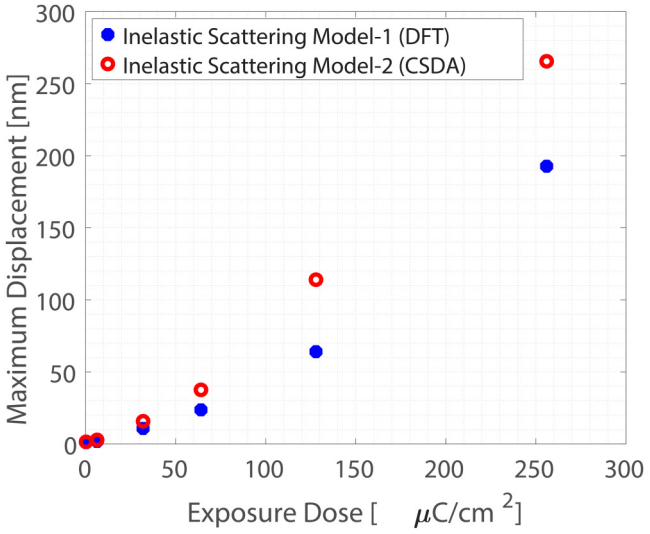

FIG. 7. Sensitivity of the displacement to the choice of the inelastic scattering model. The maximum displacement vs exposure dose in *Meander* mode shows a factor of two difference for 9 × 9 arrays.

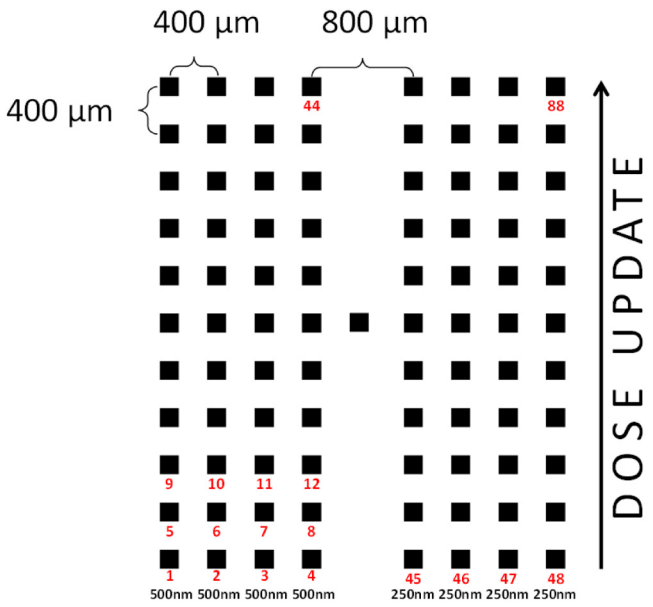

FIG. 8. Layout of a main block consisting of dot arrays (indicated by the black squares) and a central marker. The arrays in the left four columns contain dots at a 500 nm pitch and in the right four columns at a 250 nm pitch. Moving upward along the rows, the dose increases by a factor of 1.2 The writing order of the arrays is indicated by the red numbers below the arrays.

sample was produced using a standard ($525 \pm 20\,\mu$m thick) silicon wafer (2×2 cm^2). The samples were exposed with a RAITH EPBG-5200 tool. The beam energy was 50 keV, and the beam current was 0.5 nA. The location of each dot array was reached by stage movement, to be able to write the array in the center of the so-called main field, thereby minimizing the aberrations of the main field deflectors.

After the exposure, the samples were developed in a 1:3 methyl-isobutyl ketone:isopropanol (MIBK:IPA) for 60 s, rinsed in IPA for 60 s and dried with dry nitrogen gas. After development, the samples were sputter coated with molybdenum (Mo) for 8 s, corresponding to a layer thickness of ~4 nm. The conductive coating serves to eliminate possible charging effects during the subsequent inspection by scanning electron microscopy (SEM).

B. Exposure layout

The sample layout consists of four main blocks, one for each scan strategy. Each main block, shown in Fig. 8, consists of 44 arrays of 9×9 dots, 44 arrays of 17×17 dots, markers, and labels.

In a main block, the arrays of 9×9 dots, with the dots at a 500 nm pitch, were written first. The exposure starts from the

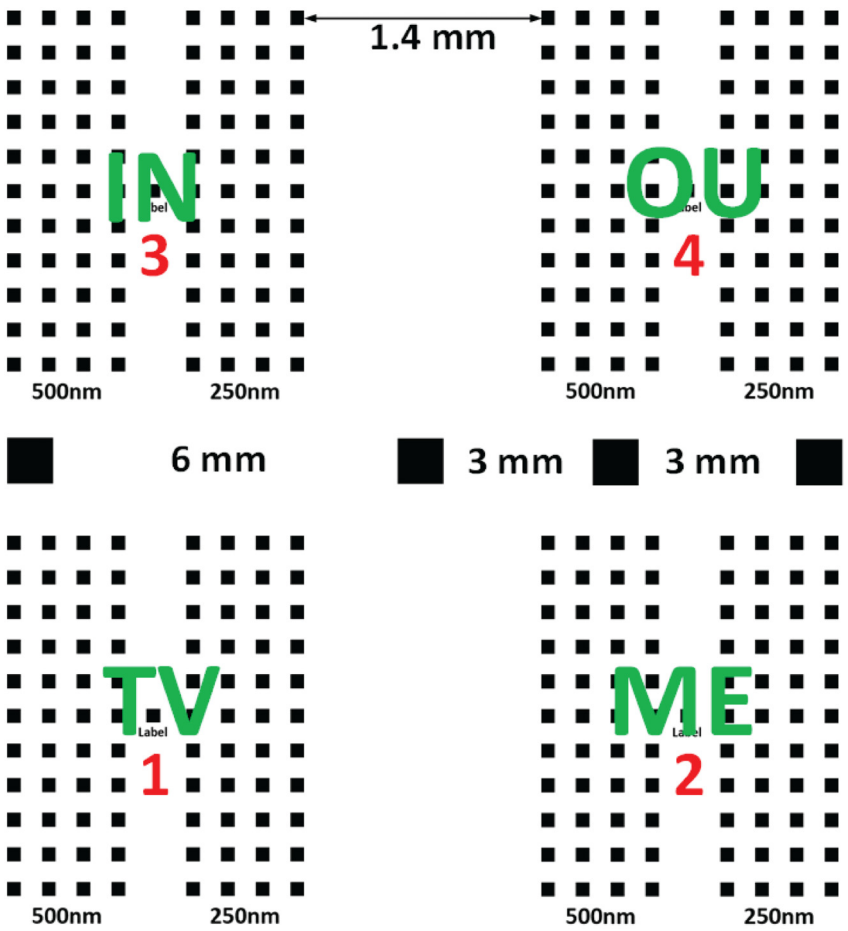

FIG. 9. Entire layout of exposed patterns on the 2×2 cm^2 wafer. The horizontal pitch of the main blocks is 1.4 mm, and the vertical pitch is 1.4 mm. The different scan modes in each main block are indicated by two letter labels: TV, ME, IN, OU (in green in the color online version). The main block writing order was TV > ME > IN > OU indicated by numbers below the scan mode (in red in the color online version).

bottom left array. The writing order is indicated by the red numbers below the arrays in Fig. 8. In each horizontal row, four arrays are written, at a 400 μm pitch, with exactly the same dose. These patterns should be nominally the same. After that, above the first row, four arrays are written at the same pitch but with a 1.2 times larger exposure dose. In this way, 11 rows are written at increasing dose. After that, 44 arrays (11 rows and 4 columns) of 17×17 dots, with dots at a 250 nm pitch, were written at 800 μm distance to the right of the first 44 arrays. The dose increase along the rows will provide information on the dose dependence of the charging effects. The four columns will give information on eventual long-range proximity effects on the charging. The latter effects will not be discussed in this work. After all arrays were written, large markers ($200 \times 200\,\mu m^2$ square) were written in *Meander* mode at 350 μC/cm^2 to facilitate optical inspection of the patterns after development. Also, $200 \times 200\,\mu m^2$ markers were written 400 μm away at the leftmost and the rightmost side of each main block for navigation during SEM inspection. These are not shown in the layout of Fig. 8.

The arrays at the bottom row were written at a dose of 50 μC/cm^2. The dose was updated by a factor of 1.2 for each pattern above, up to a dose of 310 μC/cm^2 for the uppermost row. The dose was increased by increasing the dwell time for each dot exposure. The dwell time is given by

$$DwellTime = \frac{10 \times BeamStepSize^2 \times Dose}{Current}, \quad (1)$$

where *Beam Step Size* is the pitch of the dots in micrometer, *Dose* is the exposure dose in μC/cm², *Current* is the beam current in nA, and *Dwell Time* is the time spent per dot in microsecond.

The entire layout of all exposed patterns written in all four scan modes is shown in Fig. 9. The main blocks are labeled according to the scan strategy within the arrays (the text with big fonts in the middle of main blocks, the green text in the color online version) and the writing order of the main blocks (the numbers just below the scan strategy label, the red numbers in the color online version).

C. Inspection

The patterns were inspected in a Raith "eLINE Plus" system equipped with an interferometric stage which allows automated inspection. At first, the operator needs to locate the positions of three markers on the sample to be able to determine the absolute position of patterns on the sample. During the setting up procedure, the operator calibrates the beam focus on the markers. Once the setup is done, the tool automatically moves to predetermined coordinates of patterns, automatically focuses the beam, and takes images of the patterns. Each structure was inspected only once (unless stated otherwise) to prevent beam-induced damage[31–33] during SEM inspection (Fig. 10).

All inspections were done with an 8 keV beam and a 15 μm aperture and at a working distance of 6.4 mm. The field of view was 12 μm. The brightness and contrast values were 50.1% and 31.4%, respectively, and the InLens detector of the GEMINI column was used.

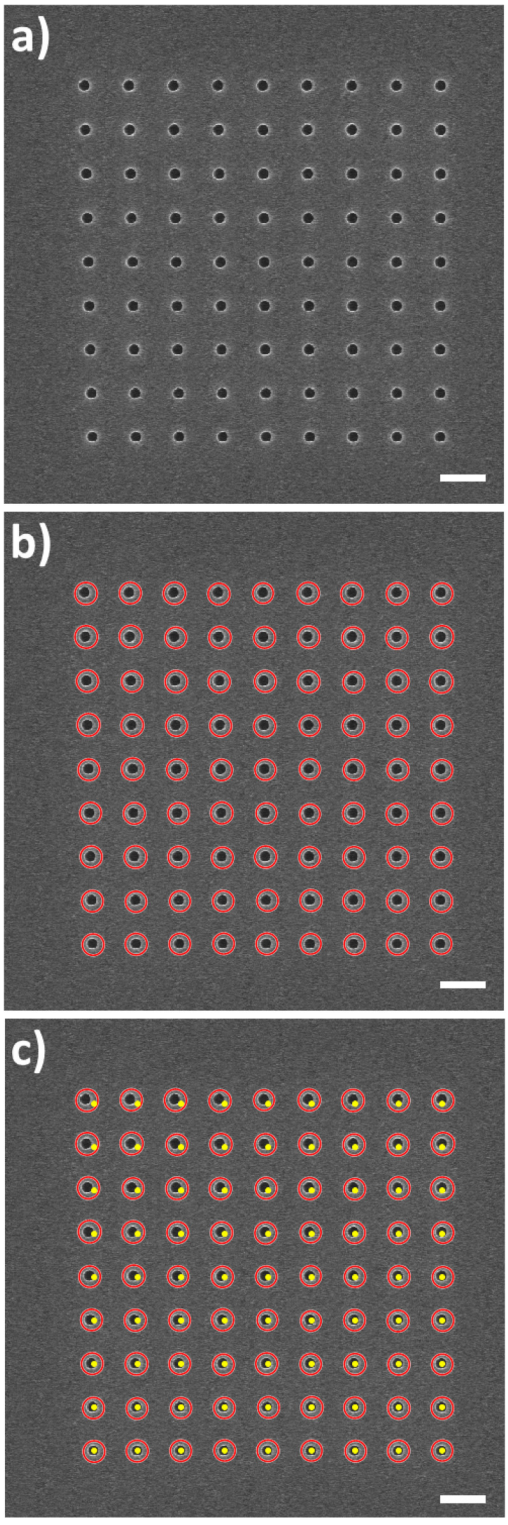

FIG. 10. Example of dot detection. The scale bars are 500 nm. (a) An SEM micrograph of a 9×9 dot pattern written in Meander mode at 124 μC/cm^2; (b) the detected dots, marked by (red - in the color online version) circles; (c) the image of (b) overlaid with the intended dot pattern marked by (yellow - in the color online version) dots. The charge-induced displacements are clearly seen.

D. Image processing

We have processed the images with a MATLAB script which can be found in the supplementary material.[35] The script covers the following image processing steps: (i) noise

filtering based on a median filter (with a 9×9 square window) to preserve the feature edges and a sophisticated contrast adjustment based on adaptive histogram equalization,[34] (ii) dot pattern recognition by using a disk shape structural element, (iii) determination of the center of mass of for each dots, and (iv) comparison of the detected dot pattern with the designed dot pattern.

Once the dot positions are detected, the pattern is compared with the predetermined pattern, using the first exposed dot as a reference point. We assume that this dot is not affected by any beam-induced effect because there has not been any electron exposure nearby.

IV. RESULTS

The simulation shows that the charging can deflect the beam by more than a few hundred nanometers at 50 keV, and the displacement of the exposed dots increases when the exposure dose increases (see Fig. 7). The simulations also demonstrate that the impact of the scan strategy is significant (see Fig. 4). For the *Meander* and *TV* modes, the simulations and experiments show very similar trends, and even the magnitudes of the maximum displacement agree very well, as demonstrated in Fig. 11.

Simulations and experiments were also compared at different doses to demonstrate the effect of the exposure dose. For example, at lower doses, such as $\sim 60\,\mu C/cm^2$, the quantitative match is less good, but qualitatively they still match, as seen in Fig. 12.

For the *Outward Spiral* and *Inward Spiral* modes, we observe more significant differences between the simulations and the experiments. In Fig. 13, the simulation result for the *Outward spiral* mode, at a dose of $128\,\mu C/cm^2$, is compared with experiments at two different doses. In the simulation, the magnitude of the displacement increases when more and more charge is deposited, taking its largest value at the bottom leftmost dot. The experimental result at $124\,\mu C/cm^2$ shows both a qualitative and quantitative mismatch to the simulation. Specifically, the displacement at the top border is negligible and

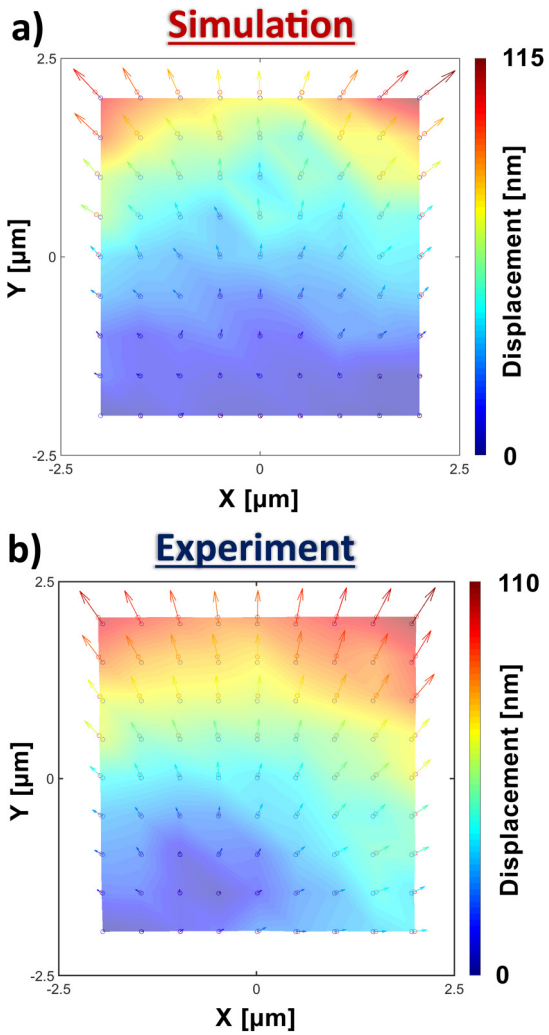

FIG. 11. Comparison between (a) simulation at $128\,\mu C/cm^2$ and (b) experiment at $124\,\mu C/cm^2$ for the *Meander* mode for a 500 nm dot pitch at $128\,\mu C/cm^2$.

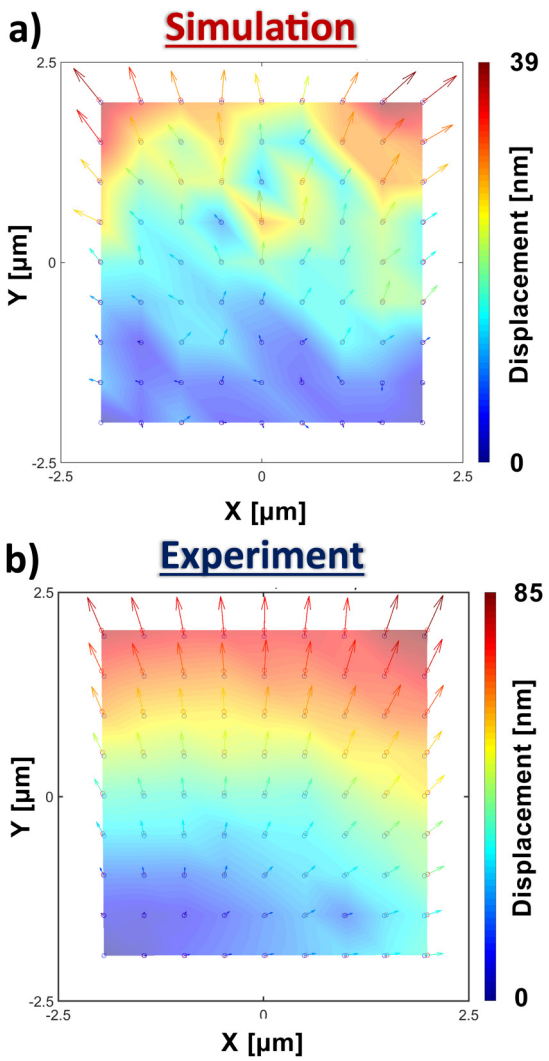

FIG. 12. Comparison between (a) simulation at $64\,\mu C/cm^2$ and (b) experiment at $60\,\mu C/cm^2$ for the *Meander* mode for a 500 nm dot pitch.

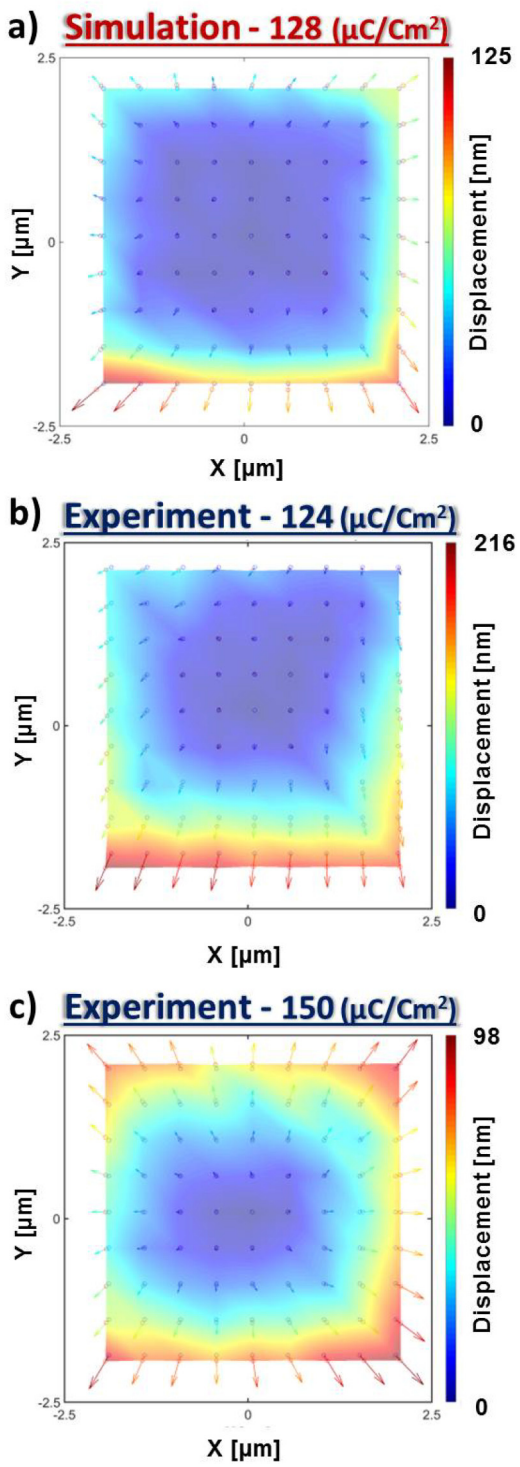

FIG. 13. Comparison between (a) simulation at 128 μC/cm^2, (b) experiment at 124 μC/cm^2, and (c) experiment at 150 μC/cm^2 for the *Outward Spiral* mode for a 500 nm dot pitch.

directed downwards. However, the experimental result at 150 μC/cm^2 matches qualitatively and quantitatively better with the simulation even though it is exposed at a higher dose: the displacement at all borders is larger than in the central area, and the maximum displacement in the experiment (98 nm) is very similar to the simulated one (125 nm).

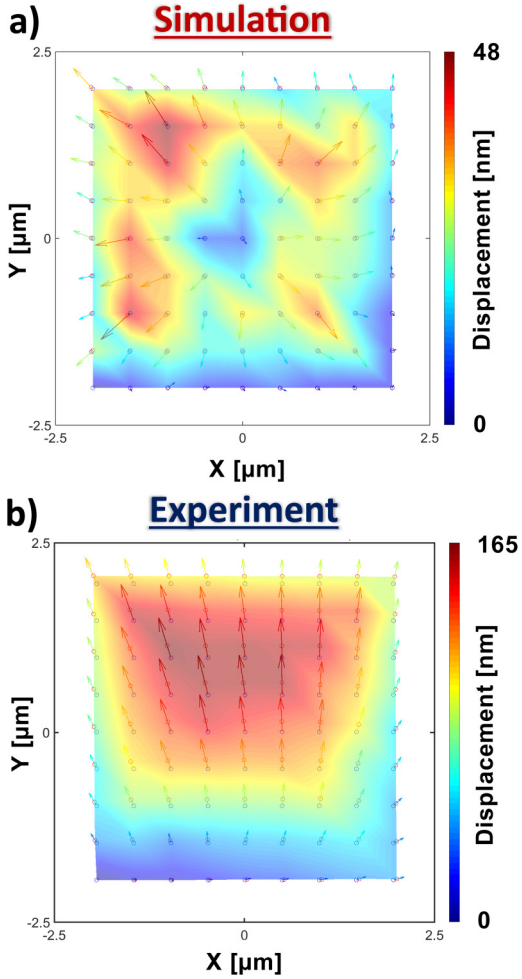

FIG. 14. Comparison between (a) simulation at 128 μC/cm^2 and (b) experiment at 124 μC/cm^2 for the *Inward Spiral* mode for a 500 nm dot pitch.

Figure 14 compares the simulation and experiment written in *Inward Spiral* mode. As discussed in Sec. II C, the displacement at the borders is limited in this writing mode as the charging is not strong enough to deflect the beam noticeably. However, the displacement maps do not match well at all. A similar mismatch also shows at other doses, although the experimental maximum displacement is somewhat closer, by a factor of ~2, to the simulation result.

Figure 15 compares the simulation and the experiment, also for the *Inward Spiral* scan mode, but at a smaller dot pitch (250 nm). At this pitch, a much better match is observed between experiment and simulation. Furthermore, the amount of displacement also matches quite well.

Finally, we verified the expected influence of the charging on the dot size, originating from the increasing beam deceleration toward the last written dots. This effect should be more prominent at a higher dose than at a lower dose. In Fig. 16, the diameters of the dots in the top and bottom rows of a 9×9 array of dots, written in *Meander* mode, are compared for a dose of 50 and 258 μC/cm^2. At a dose of 50 μC/cm^2, the mean diameters of dots in the top and bottom rows are almost equal (80.7 vs 80.6 nm). At a dose of 258 μC/cm^2, the phenomenon is

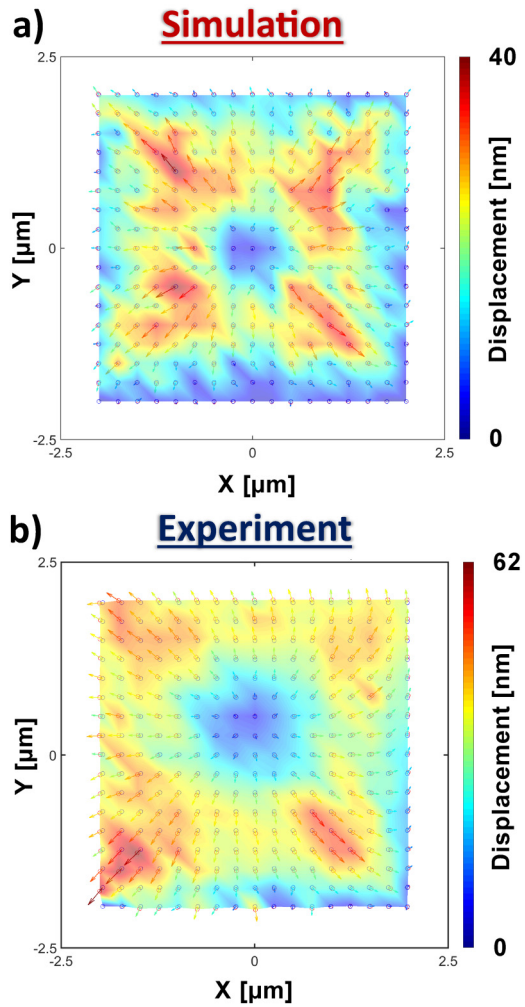

FIG. 15. Comparison between (a) simulation at 128 μC/cm^2 and (b) experiment at 124 μC/cm^2 for the *Inward Spiral* mode for a 250 nm dot pitch.

distinguishable. The mean diameter of the top row dots is 103.1 nm where the bottom row dots have a mean diameter of 98.7 nm. This demonstrates the effect of charging on feature sizes.

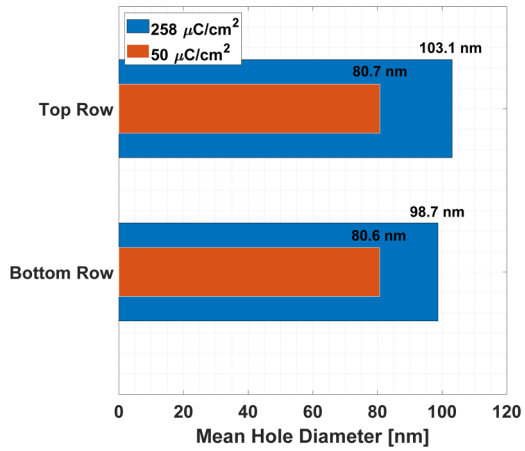

FIG. 16. Effect of charging on dot diameters. The mean diameters of the top and bottom row dots are compared for a low (50 μC/cm^2) and a high (258 μC/cm^2) exposure dose for a 9 × 9 dot array written in *Meander* mode.

V. CONCLUSIONS

From the simulations, we predicted significant charging effects during EBL on glass wafers at 50 keV. These were also experimentally verified. Beam displacements as large as a few hundred nanometers, depending on the exposure dose, were observed, as well as charge-induced feature size changes. These, especially the beam displacement, pose a serious problem for accurate patterning of high-end structures and call for ways to minimize these effects.

From simulations, we concluded that the scan strategy influences pattern shapes. We tested four different scan strategies and found that a smart strategy, such as the *Inward Spiral* mode, can minimize the deformation of square patterns showing the power of simulations to identify the right strategy for a certain pattern shape. Although some experimental cases (like Fig. 14) deviate, the possibility of minimizing the deformations by a smart scan strategy was supported by most of the experiments.

We have also observed unexpected deviations between experiments and simulations such as shown in Fig. 13. These deviations decreased when increasing the exposure dose, resulting in a better qualitative match and less displacement. This is not understood yet but perhaps arises from possible errors in the entire process (exposure, inspection, and postprocessing). There is no reasonable physical explanation of why all the displacement arrows at the top of the middle image of Fig. 12 point downwards. The simulations did not show such dose-dependent, unexpected, changes in the displacement maps. The fact that such effects were observed in the experiments prevents us from drawing definite conclusions on the influence of the scan strategy and these should be investigated in further study. However, the qualitative agreement, and even sometimes the quantitative agreement, between the experiments and the simulations is remarkable. CSDA model was used for all simulations in the experimental comparisons to reduce the simulation time. It is noted here that there is an influence of the inelastic scattering model used on the magnitude of the displacements, which can amount up to a factor of 2. However, the relatively good agreement between the simulations and experiments is encouraging to make use of Monte Carlo simulations to predict the influence of charging in EBL, but also in SEM imaging.

The beam displacement phenomenon in EBL, leading to observable displacements of exposed dot patterns, is a valuable test case for the simulation of charging. It allows collecting data on charging phenomena in a much more controlled way than analysis of SEM images of charging samples, and it also avoids complexities caused by surface topography.

ACKNOWLEDGMENTS

The first author is grateful to Pieter Kruit, for discussions on the charging phenomenon and nanofabrication; Wilco Zuidema and Marco Wisse, for discussions on imaging processing; and Martin Kamerbeek, for discussions on the sample preparation for SEM inspection and nanofabrication. The authors acknowledge GenISys-GmbH and RAITH B.V. for funding this research project.

[1]I. Charaev, A. Dane, A. Agarwal, and K. K. Berggren, IEEE Trans. Appl. Supercond. **29**, 1 (2019).
[2]Y. Chen, Microelectron. Eng. **135**, 57 (2015).
[3]A. E. Grigorescu and C. W. Hagen, Nanotechnology **20**, 292001 (2009).
[4]V. R. Manfrinato, L. Zhang, D. Su, H. Duan, R. G. Hobbs, E. A. Stach, and K. K. Berggren, Nano Lett. **13**, 1555 (2013).
[5]V. R. Manfrinato *et al.*, Nano Lett. **14**, 4406 (2014).
[6]M. Rommel and B. A. Nilsson, Microelectron. Eng. **155**, 29 (2016).
[7]K. D. Cummings, J. Vac. Sci. Technol. B **7**, 1536 (1989).
[8]A. Aassime, F. Hamouda, I. Richardt, F. Bayle, V. Pillard, P. Lecoeur, P. Aubert, and D. Bouchier, Microelectron. Eng. **110**, 320 (2013).
[9]Ş Tirpanci, D. E. Bürgler, C. M. Schneider, B. Rameev, and B. Aktaş, Microelectron. Eng. **140**, 33 (2015).
[10]B. Leibold, J. Butschke, L. Bettin, D. Beyer, M. Irmscher, C. Koepernik, R. Plontke, A. Vix, and P. Voehringer, Proc. SPIE **5256**, 1034 (2003).
[11]R. Abargues, U. Nickel, and P. J. Rodríguez-Cantó, Nanotechnology **19**, 125302 (2008).
[12]B. D. Myers and V. P. Dravid, Nano Lett. **6**, 963 (2006).
[13]J. Joo, B. Y. Chow, and J. M. Jacobson, Nano Lett. **6**, 2021 (2006).
[14]R. Pintus, S. Podda, and M. Vanzi, IEEE Trans. Instrum. Meas. **57**, 989 (2008).
[15]H. Itoh, J. Vac. Sci. Technol. B **9**, 3039 (1991).
[16]J. Zhang, M. Fouad, M. Yavuz, and B. Cui, Microelectron. Eng. **88**, 2196 (2011).
[17]R. J. Hawryluk, H. I. Smith, A. Soares, and A. M. Hawryluk, J. Appl. Phys. **46**, 2528 (1975).
[18]J. J. Hwu and D. C. Joy, Scanning **21**, 264 (1999).
[19]J. J. Hwua, Y. Ko, and D. C. Joyatb, Control **3998**, 239 (2000).
[20]Y. Ko, J. J. Ha, and C. David, Proc. SPIE **3998**, 694 (2000).
[21]K. T. Arat, T. Klimpel, and C. W. Hagen, Proc. SPIE **10585**, 43 (2018).
[22]K. T. Arat, J. Bolten, T. Klimpel, and N. Unal, Proc. of SPIE **9778**, 97780C (2016).
[23]E. Kieft and E. Bosch, J. Phys. D Appl. Phys. **41**, 215310 (2008).
[24]T. Verduin, "Quantum noise effects in E-beam lithography and metrology" Ph. D. thesis (Delft University of Technology, 2016).
[25]Y. Lin and D. C. Joy, Surf. Interface Anal. **37**, 895 (2005).
[26]K. D. Cummings, J. Vac. Sci. Technol. B **8**, 1786 (1990).
[27]H. J. Fitting, H. Glaefeke, and W. Wild, Phys. Status Solidi **43**, 185 (1977).
[28]N. Cornet, D. Goeuriot, C. Guerret-Piécourt, D. Juvé, D. Tréheux, M. Touzin, and H.-J. Fitting, J. Appl. Phys. **103**, 064110 (2008).
[29]M. Aktary, M. Stepanova, and S. K. Dew, J. Vac. Sci. Technol. B **24**, 768 (2006).
[30]Q. Dai, S. Y. Lee, S. H. Lee, B. G. Kim, and H. K. Cho, Microelectron. Eng. **88**, 3054 (2011).
[31]J. J. Ritsko, L. J. Brillson, R. W. Bigelow, and T. J. Fabish, J. Chem. Phys. **69**, 3931 (1978).
[32]R. F. Egerton, S. Lazar, and M. Libera, Micron **43**, 2 (2012).
[33]R. F. Egerton, P. Li, and M. Malac, Micron **35**, 399 (2004).
[34]K. Zuiderveld, *Graphics Gems IV*, edited by P. S. Heckbert (Academic, San Diego, CA, 1994), pp. 474–485.
[35]See supplementary material at https://doi.org/10.1116/1.5120631 for a file that contains a MATLAB script for analysis of SEM micro-graphs of the study.